scientific reports

Check for updates

OPEN

CO_2 dissolution-diffusion in clay inhibitor/oil systems and synergistic CCUS-EOR effects in strongly water-sensitive reservoirs

Miaoxin Zhang[1], Jingchun Wu[1]✉, Liyuan Cai[1], Bo Li[1], Xin Yu[1], Yangyang Hou[1], Fang Shi[1] & Chunlong Zhang[2]

This study targeted a highly water-sensitive reservoir with high clay content (average 23.87%, mainly montmorillonite and illite), where waterflooding development induces hydration swelling of clay minerals, leading to pore-throat narrowing. The anti-swelling system and CO_2 were found to mitigate this phenomenon. The research investigated the dissolution, diffusion, and synergistic effects of CO_2 in the anti-swelling system/crude oil within the context of Carbon Capture, Utilization and Storage-Enhanced Oil Recovery (CCUS-EOR). Using the pressure decay method, core flooding experiments, microscopic visualization of oil displacement, and an improved mathematical model. We systematically investigated the influence of clay minerals on the balance between CO_2 storage and enhanced oil recovery (EOR). It was found that the diffusion coefficient of supercritical CO_2 increased rapidly and then levelled off with increasing pressure, which indicated that clay minerals hindered CO_2 diffusion. The anti-swelling system increases the effective pore connectivity by suppressing clay swelling, which increases the diffusion coefficient by 20–28%. The enhanced mathematical model combines the oil-water phase partition coefficients with the PR-EOS equation of state to accurately describe the multiphase interactions. The calculation results fit the experimental data by 92%, which is better than the traditional single-phase model. Through microscopic oil displacement experiments, core flooding tests, and quantitative analysis of full-cycle CO_2 saturation evolution. It is demonstrated that the sweep efficiency is anti-swelling system-CO_2 flooding is a higher sweep efficiency (73.95%) and achieves 58.12% oil recovery and 46.16% CO_2 sequestration efficiency in a core with a permeability of 102.95×10^{-3} μm². The full-cycle CO_2 saturation change rule was quantified, and the saturation cloud map was drawn. It is proven that the technology has the synergistic mechanism of 'stabilising pore structure-reducing oil viscosity-efficient sequestration', which combines significant oil recovery and carbon sequestration benefits, and provides theoretical and practical guidance for the low-carbon development of strong water-sensitive oilfields.

Keywords CCUS-EOR, Strongly water-sensitive reservoirs, Clay minerals, Carbon sequestration, Enhanced oil recovery

Abbreviations

CCUS-EOR	Carbon Dioxide Capture, Utilisation and Storage with Enhanced Oil Recovery
C_{eq}	CO_2 concentration at the equilibrium pressure P_{eq}
K	the mass transfer coefficient at the gas-liquid interface
D_{eff}	diffusion coefficient
r0	radius
T	time
$\overline{r_0}$	length
u	velocity
$\overline{c}$	average concentration

[1]Key Laboratory for EOR Technology (Ministry of Education), Northeast Petroleum University, Daqing 163318, China. [2]Daqing Yongzhu Petroleum Technology Development Co Ltd, Daqing 163000, China. ✉email: w6529@163.com

C_0	initial concentration
C_i	concentration at time i
k_{pco} and k_{pcw}	partition coefficients for carbon dioxide concentrations in the oil and aqueous phases
Δ_{ng}	reduction of carbon dioxide in the gas phase
Z	gas deviation factor
R	gas constant
Q	amount of gas lost in the gas phase at time t
P_o	initial pressure of gas before diffusion
ΔV	volume reduction of the gas phase

With the rapid development of the global economy, the rapid consumption of fossil energy, and the continued emission of greenhouse gases, the world is facing a climate change crisis. The innovation and development of CCUS-EOR (Carbon Dioxide Capture, Utilisation and Storage with Enhanced Oil Recovery) technology[1–5] is crucial to guarantee the promotion of carbon emission reduction and carbon neutrality targets while ensuring the diversity of energy structure.

The development technology for gas injection in conventional sandstone reservoirs has been continuously refined and improved based on prior research findings. This has led to the establishment of a comprehensive technological system for carbon capture, utilization, and storage[6–9]. Conventional CCS reservoirs are mainly targeted at porous rock formations, such as sandstones and carbonate aquifers, with predominantly primitive porosity[10–12]. The search for potential CO_2 storage reservoirs has now expanded to non-traditional geological environments. Specifically, this includes carbonate reservoirs with naturally occurring fractures. Additionally, residual oil zones (ROZ) and shale reservoirs may also emerge as new CO_2 storage sites[13–16].

The strong water-sensitive reservoir studied in this paper is characterized by high clay mineral content and strong sensitivity to external fluids[13,14]. The use of conventional water flooding is prone to induce hydration and expansion of clay minerals, reduce pore connectivity, and lead to an increase in injection pressure, which prevents the establishment of an effective flooding system. Unlike[15–17] which focused on traditional sandstones, this study targets reservoirs with high clay content and water-sensitive properties. Based on the swelling and instability of clays in porous media, the diffusion characteristics of CO_2 and its performance in displacing crude oil were further investigated. Although the properties of CO_2 can effectively avoid this negative effect of strongly water-sensitive reservoirs[18,19] the high content of clay minerals has a strong adsorption effect on CO_2, and the interaction effect between CO2 and the crude oil in the pore space is weakened, resulting in relatively low recovery and carbon sequestration efficiency[20–22]. However, the synergistic effect of the anti-swelling system and CO_2 can achieve multiple effects of stabilising the pore space structure, enhancing the ability to replace crude oil, and reinforcing the effect of carbon sequestration. Sequestration effect. The synergistic effect of CO_2 and the anti-swelling system proposed in this study can simultaneously achieve enhanced crude oil recovery and carbon dioxide sequestration efficiency, providing a new idea for energy and environmental security.

CO_2 flooding offers unique advantages for water-sensitive reservoirs by avoiding clay hydration swelling, a critical limitation of conventional water flooding[5,23,24]. Unlike water, CO_2 does not induce montmorillonite expansion, maintaining pore connectivity[13]. However, high clay content (23.87% average in this study) enhances CO_2 adsorption (2.35 mmol/g for montmorillonite[21,25]), reducing diffusion efficiency by 40% compared to clay-free cores. Prior studies[8,26] focused on conventional sandstones, lacking insights into clay-CO_2 interactions in reservoirs where swelling-induced pore plugging reduces permeability[14].

The reasons why the existing technology does not apply to the reservoir studied in this paper are as follows: ① The low mineralisation of low-mineralised water will lead to hydration and expansion of clay minerals in the pore channel and blockage of the seepage channel.② Micro and nano bubbles are with water as the continuous phase and CO_2 as the dispersed phase; the reason is similar to low mineralised water flooding.③ CO_2 viscosity enhancement technology has a limited viscosity enhancement effect, and the concentration of added chemical reagents and additives is high, and the cost increase is large; therefore, it is not considered.④ CO_2 foam flooding technology is applied to conventional sandstone reservoirs, which has a better effect of controlling the driving front and expanding the sweep efficiency, but the reservoir in this study has a high content of clay minerals, and the surfactant is adsorbed on the pore wall, which leads to a deterioration of the oil flooding effect. Previously, the main research direction for water-sensitive reservoir mining technology was to reduce the swelling effect between aqueous solution and clay by adding chemical additives[27–29]. The synergistic development of CO_2 and anti-expansion aqueous solution has not been considered for the time being. As Table 1 shows, there is a lack of research on the relationship between CO_2 and the anti-swelling system, as well as the effect of enhanced oil recovery. Therefore, to achieve the purpose of both enhanced recovery and carbon sequestration efficiency, the dissolution law of different mixed fluids needs to be further supplemented.

Given the global imperative to maintain energy security while achieving carbon neutrality, implementing CCUS-EOR technologies in water-sensitive reservoirs remains an unresolved challenge. Traditional methods fail in formations with high clay content, where water flooding causes permeability reduction and CO_2 flooding alone exhibits low storage efficiency. This study fills critical gaps by: (1) quantifying how clay in porous media hinders CO_2 diffusivity; (2) investigating a synergistic anti-swelling/CO_2 system to restore pore connectivity; and (3) integrating a mathematical model that achieves consistency with experimental results, demonstrating higher accuracy than traditional approaches. The technology stabilizes pore structures in water-sensitive reservoirs, enhancing oil recovery and prolonging CO_2 breakthrough time. This not only advances the scientific understanding of clay-CO_2-oil interactions but also provides a practical roadmap for low-carbon development in other water-sensitive reservoirs.

System			Temperature (℃)	Pressure (MPa)	Experimental sample	Diffusion coefficient ($\times10^{-9}$ m²/s)	Quote
Gas	Water	Oil					
CO_2	Brine		38	1.45–5.86	Berea sandstone	1.97–5.05	[30]
CO_2		Pitch	25–90	4,8	Diffusion vessel	0.58–1.06	[31]
CO_2		Octane	38	1.524–5.178	Diffusion vessel	2.925–4.827	[32]
CO_2+N_2		Crude oil	63	5.275–7.686	Diffusion vessel	3.67–12.51	[33]
CO_2	Brine		20	1、1.5、3	Diffusion vessel	1.28–12.91	[34]
CO_2	Brine		32–50	5.9–6.9	Diffusion vessel	3.52–6.16	[35]
CO_2		Tetradecane	38	1.905	Diffusion vessel	0.478–1.706	[36]
CO_2		White oil	136.85	7.096	Diffusion vessel	3.351–4.83	[37]
CO_2	Brine		59	2.4–7.3	Sandstone(80–1527mD)	3.14–6.51	[38]
CO_2		Crude oil	40	2.28–6.5	Sandstone(163–263mD)	5.98–8.01	[39]

Table 1. Example of carbon dioxide diffusion experiment.

Rock type	Permeability ($\times10^{-3}$μm²)	Porosity (%)	Formation depth (m)	Saturation conditions (%)	Clay content (%)
Argillaceous siltstone	3–28	14.5–15.8	826–839	46–53	15.73–44.09

Table 2. Physical properties of the reservoir.

Experimental material	Deionized Water V_w(mL)	Experimental Photo	Kerosene V_o(mL)	Experimental Photo	Anti-Swelling System V_a(mL)	Experimental Photo	Anti-Swelling Rate B(%)
Montmorillonite and illite	7.8		0.52		0.9		94.09

Table 3. Clay inhibitor anti-swelling effect.

CO_3^{2-}	HCO_3^-	Cl^-	SO_4^{2-}	Ca^{2+}	Mg^{2+}	K^+/Na^+
278	3310	1300	60	44.1	15.8	2250

Table 4. Brine ion content (mg/L).

Experimental component

Experimental materials

Experimental conditions: temperature 42 °C, reservoir pressure 10.5 MPa.

Experimental agents: potassium chloride, methanol, anhydrous ethanol, ethylene glycol, clay inhibitor, complex surfactant, etc. Clay inhibition system formulation: quaternary ammonium clay inhibitor 1% + polyethylene glycol + 0.3% non-ionic surfactant + 1% inorganic salt.

Experimental oil: crude oil. The saturation pressure is 5.16 MPa, the formation volume factor is 1.08, the viscosity is 17.64 mPa·s, the gas-oil ratio is 19.51 m³/t, the molecular weight of crude oil is 505.27, and the formation oil density is 0.803 g/cm³.

Experimental core: natural core of the target area (mainly siltstone or muddy siltstone, with an average clay content of 23.87%, mainly montmorillonite, ilmenite, and kaolinite; the water sensitivity index ranges from 88 to 98%). The permeability of the main oil reservoir is approximately 10×10^{-3} μm². Core parameters are shown in Table 2.

Experimental water: The anti-swelling system consists of 1% polyethylene glycol + 0.3% non-ionic surfactant + 1% inorganic salt stabilizer. The performance of the anti-swelling system is shown in Table 3. The formulation of the simulated formation water is listed in Table 4.

Experimental gas: simulated natural gas and CO_2 (purity 99.9%), as shown in Table 5.

Component	Volume fraction%	Component	Volume fraction%	Component	Volume fraction%
Methane	91.274	Isobutane	0.216	N-pentane	0.136
Ethane	1.932	Butane	0.528	hexane	0.030
Propane	1.609	Isopentane	0.080	nitrogen	4.195

Table 5. Natural gas fractions.

Apparatus

Thermostatic box, high-pressure diffusion bucket, HTP-3 A high-temperature and high-pressure expansion instrument, TGL-16G high-speed centrifuge, high-temperature and high-pressure PVT, ISCO pump, pressure-resistant intermediate vessel, gas-liquid separator, gas chromatography/mass spectrometer, back pressure valve, one-way valve, Brinell viscometer, beaker, measuring cylinder, etc.

Methods

Dissolution diffusion experiment

The diffusion coefficient of CO_2 was measured using a PVT cylinder via the pressure decay method, with calculations based on Fick's second law to characterize mass transport behavior in porous media. The experimental design aimed to replicate in-reservoir conditions for accurate diffusion parameterization, as follows: (1) Transfer fluids into the PVT cell in proportion according to the experimental protocol, and heat the cell to reach the reservoir pressure and temperature conditions. (2) Transfer the prepared gas sample into the upper part of the PVT cell from the top using an equilibrium sample transfer method to prevent convective mixing during the transfer process. (3) Conduct the diffusion experiment and record the data on time and pressure. The experiment is considered complete when the pressure change is less than 0.1 MPa within 1 h. (4) Press the fluids in the PVT cell into a flash separator, and record the volumes of the liquid and gas phases, respectively. (5) Calculate the solubility, summarize the data, and plot graphs.

The temperature of the high-pressure physical properties analyser was kept constant at 42 °C, a quantitative amount of M_0 liquid was injected into the PVT cylinder of the analyser in vacuum, CO_2 was injected into the PVT cylinder, and stirring under pressure caused the gas to dissolve in the liquid, and the dissolved gas-liquid ratio was calculated using the formula $GOR = V_g/M_o$. Simulated high-salinity water was prepared by dissolving reagents[40]including NaCl, $CaCl_2$, $MgCl_2$, and so on. With a total salinity of 7260 mg/L. The ionic composition is presented in Table 4. The preparation of the anti-swelling system was described in the experimental water section of Sect. 1.1.

Dissolution and diffusion experiment in rock core

Diffusion experiments were performed on core samples under varying pressures, oil saturations, and permeabilities to characterize CO_2 transport behavior in reservoir conditions. The experiments were designed to isolate the effects of key reservoir parameters on diffusion kinetics, with core samples sourced from low-permeability formations featuring high clay content. The average permeability of the core is about 10×10^{-3} μm^2, and the porosity is about 15–16%. The experimental steps are as follows: (1) Arrangement of the cores based on gas permeability and arrangement formulae. (2) Vacuuming with a vacuum pump for more than 6 h, saturating the core with 3% KCL brine, and measuring pore volume and permeability. (3) Formation of crude oil compounding with high temperature and high pressure PVT under reservoir conditions. (4) Saturate and age the formation crude oil under reservoir conditions and calculate initial oil saturation, bound water saturation, and gas-oil ratio. (5) Open the connecting valves of the CO_2 high-pressure vessel and core gripper and collect data through the pressure sensor. The pressure measurement precision was 0.01 MPa, and the time measurement precision was 0.1 s. (6) End the experiment when the diffusion process reaches a steady state, release the pressure in sections, and disassemble and clean the experimental setup. (7) Calculate the dissolved diffusion coefficient of CO_2 based on Fick's second law and summarise the experimental data.

Fick's second law states that in unsteady-state diffusion, the rate of change of concentration with time at a distance x from the gas-liquid interface in the liquid phase is equal to the negative of the spatial derivative of the diffusion flux, described by the equation: $\frac{\partial C}{\partial t} = -\frac{\partial}{\partial x}\left(D\frac{\partial C}{\partial x}\right)$. Here, C denotes concentration, t is time, x is the spatial coordinate, and D represents the diffusion coefficient. The law mathematically links the temporal evolution of concentration to the spatial gradient of diffusive flux, emphasizing the non-steady nature of mass transport processes. The effective diffusion coefficient(D_{eff}) is described by the equation: $D_{eff} = \frac{\varnothing}{\tau}D$, where $\varnothing$ is the porosity, τ is the tortuosity, and D is the diffusion coefficient.

Microscale oil displacement experiment

Microscopic visualization experiments were designed to investigate the dynamic mechanisms of fluid transport at the pore scale, aiming to elucidate the influence of pore structure and fluid properties on displacement efficiency. Such experiments enable direct observation of fluid flow paths and interfacial interactions under controlled conditions, providing mechanistic insights into multiphase flow behavior in porous media. The experimental steps are as follows: (1) Make a microscopic model with an injection end and a withdrawal end at the diagonal edges[41]. (2) Dry the microscopic model and then saturate the simulated formation water with a microsyringe pump, and then saturate the simulated oil, avoiding a large number of bubbles in the saturation process. (3) According to the programme, inject the microscopic model at a constant rate, and observe the micro-seepage process of the collection system in real time, and the injection rate is 0.01 mL/min. (4) According

to the changes of crude oil morphology in the microscopic model at different time stages, analyse and summarize the replacement characteristics of different injection systems. The photolithographic glass micromodel used in the experiment had a planar dimension of 10 cm × 10 cm, a thickness of 0.2 cm, and a pore volume of 2 mL.

Study of synergistic effects of enhanced recovery and carbon sequestration

Long-core flooding experiments using natural core samples were conducted to evaluate the dynamic recovery performance of different injection strategies under reservoir conditions, aiming to simulate crude oil mobilization in real reservoir environments and ensure data consistency with field-scale processes. The experimental procedure is shown in Fig. 1.Cores with similar physical properties in the target block were selected and arranged into long cores of about 1 m length according to the arrangement formula[42].(1)Place the core into the holder, and put a screen at the arrangement place to reduce the end face effect.(2)Vacuum the core and saturate it with formation water, calculate the pore volume of the core, and leave it at a constant temperature for 24 h.(3)Saturate the formation crude oil, calculate the saturated oil volume and oil saturation degree, and age at constant temperature for 24 h after saturation.(4)Set the ISCO pump to constant flow mode, with a flooding rate of 0.1 mL/min, and set the back pressure at the outlet end to the formation pressure[43].(5)Carry out oil expulsion experiments in different ways according to the design of the experimental scheme, record the data, analyse the changes in the degree of extraction during the expulsion process, stop the experiment when the water content reaches 98% or the gas-oil ratio reaches 1500m^3/m^3, and draw the dynamic change curve[44].

Results and discussion

CO_2 dissolution and diffusion law experiment

Solubility of single-phase fluids

Since the reservoir studied in this paper is a sandstone reservoir with high clay content, it has certain special characteristics. The interaction between the reservoir and the aqueous solution results in the phenomenon of hydration and expansion, which changes the pore structure of the reservoir, leading to a greater resistance to seepage and the inability to establish an effective flooding system. Therefore, the aqueous solution used in this study is an anti-swelling system. Firstly, the single-phase solubility of reservoir crude oil, brine, and anti-swelling system was separately explored in a high-temperature and high-pressure PVT reactor. Then, different water-

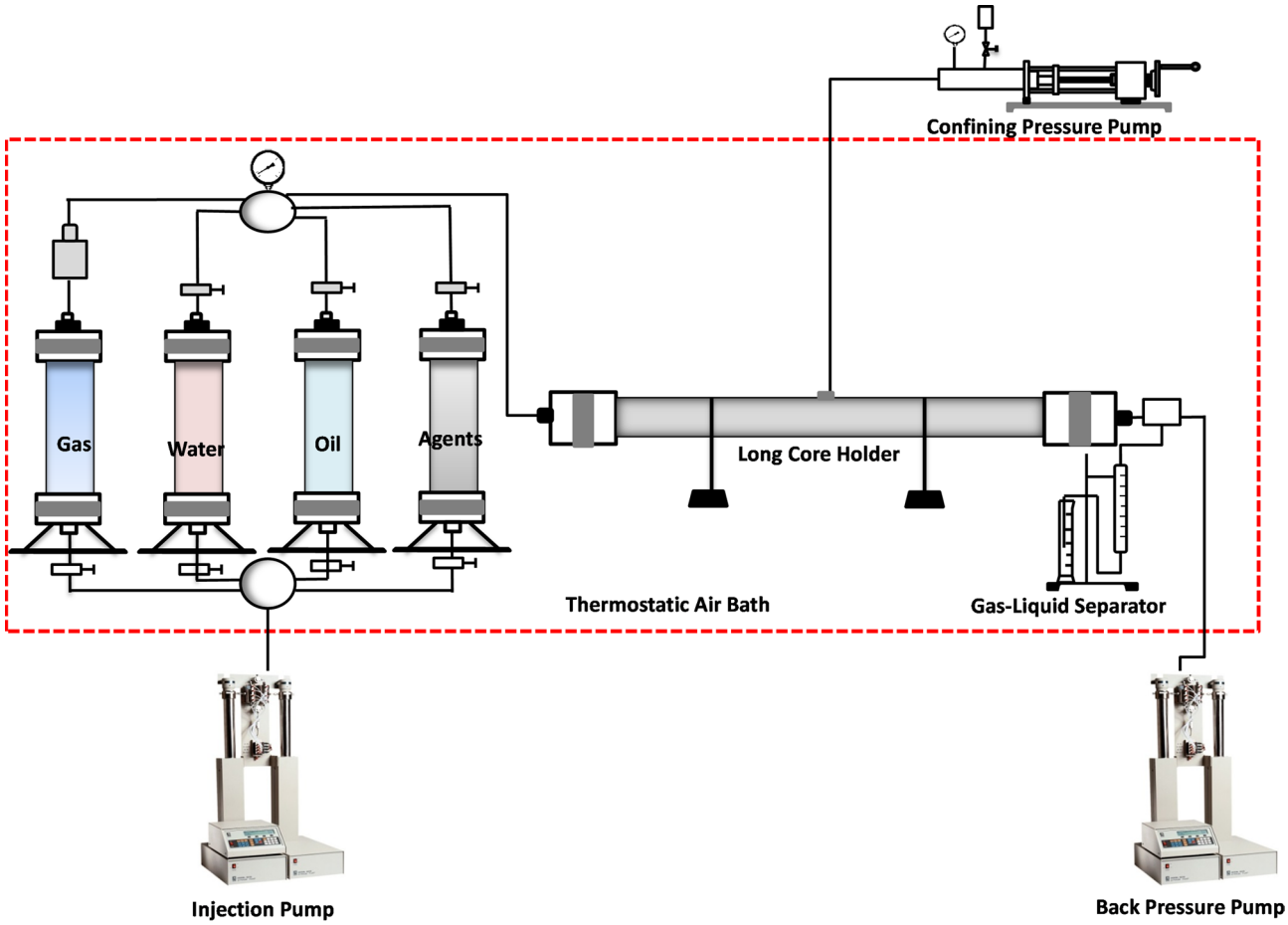

Fig. 1. Process of displacement experiment.

bearing phases of the reservoir were simulated to compare the CO_2 solubility under different oil-water and oil-agent ratio conditions.

From the experimental results in Fig. 2, three key insights were derived with explicit links to enhanced oil recovery (EOR) and CO_2 sequestration objectives: First, the solubility of CO_2 in all three fluids (oil, anti-swelling system, brine) increased with pressure, but the magnitude differed significantly. Solubility comparisons among three fluid phases revealed that the CO_2 solubility in oil, brine, and the anti-swelling system was 6.346, 0.875, and 1.232 mol/L, respectively. The experimental results were consistent with previous studies[30,33,35]. This trend directly supports EOR feasibility: the high CO_2 solubility in oil promotes in-situ viscosity reduction (by 35–40%)[24], enhancing fluid mobility and sweep efficiency. The preferential dissolution in hydrocarbons also facilitates oil swelling, which expands the oil phase volume and improves displacement efficiency in pore throats. Second, analyzing the phase behavior at Psc revealed that CO_2 solubility in the anti-swelling system exceeded that in brine by 39.6%. This enhancement is attributed to the system's organic components (e.g., polyethylene glycol), which disrupt water molecular clusters and create more favorable microenvironments for CO_2 dissolution. For sequestration, this higher solubility implies greater CO_2 storage capacity in the aqueous phase, particularly in clay-stabilized pores where the anti-swelling system maintains pore connectivity. Third, the solubility growth rate slowed in all fluids at elevated pressures, indicating approaching saturation. For practical applications, this suggests an optimal pressure window (10–15 MPa) where CO_2 dissolution efficiently balances oil viscosity reduction and sequestration capacity. The plateau in solubility also highlights the importance of alternating injection strategies to maximize CO_2 utilization before breakthrough.

These findings directly address the study's dual objectives: the high oil solubility drives EOR via viscosity modification, while the anti-swelling system's enhanced CO_2 retention supports long-term sequestration by stabilizing pore structures. The results align with prior studies[45–47] and provide a scientific basis for optimizing CO_2 flooding in water-sensitive reservoirs.

Solubility under oil/water coexistence conditions

In order to simulate the actual conditions of the reservoir, and considering the enhanced recovery and carbon sequestration synergy (CCUS-EOR) development approach, the experimental programme was designed to experiment with the CO_2 dissolution of crude oil/brine and crude oil/system at different ratios.

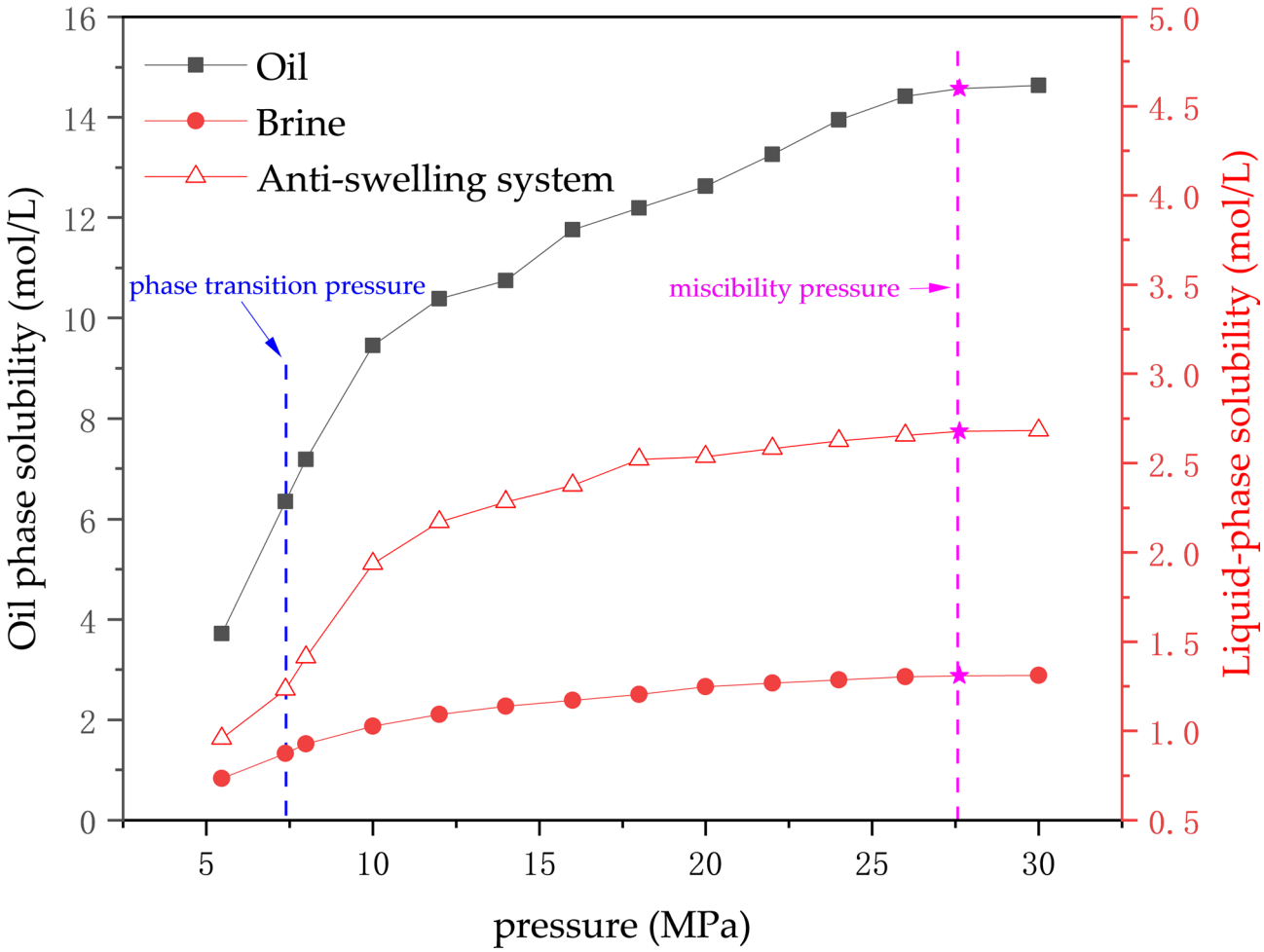

Fig. 2. Comparison of the solubility of brine, anti-bulking agent, and crude oil.

Two conclusions can be drawn from Fig. 3, The first is that under the same ratio of oil and water solution, with the increase of pressure, both mixed solutions show the trend of increasing and then levelling off, and the CO_2 solubility of oil/system is higher than that of oil-water medium.

Secondly, the difference between the two mixed solutions at different ratios of oil/water solution was compared, and it was found that as the ratio of oil in the mixed solution decreased, the CO_2 solubility decreased. However, the aqueous phase in the two mixed solutions is two media in which the proportion of the liquid phase increases as the oil ratio decreases, and the CO_2 solubility in the liquid phase increases. It was found that the difference in solubility between the two mixed liquids was maximum when the oil-water ratio was 1:9.

Dissolution and diffusion laws of CO_2/anti-expansion water in porous media

The present study compares the effects of pressure (5.61–27.53 MPa), oil saturation (0-50.16%) and permeability ($4.68\text{-}210.14\times10^{-3}$ μm^2) on the SC-CO_2 diffusion coefficient under reservoir conditions. The cores used in the experiments were natural sandstone cores with similar physical properties from the same block, and the experimental programme was designed using the controlled variable method to compare the effects of single variables[48].

Clay mineral

The diffusion coefficients of cores with different clay mineral contents (artificial core, Berea Sandstone Core, and Natural core) were measured to investigate the effects of different clay mineral types and contents on the dissolution diffusion coefficients.

As shown in Fig. 4 (a), the post-treatment core samples exhibit expanded pores, which enhance the CO_2 adsorption capacity. Figure 4 (b) compares the enhanced CO_2 diffusion coefficients of cores with different clay contents after treatment, revealing an increase of approximately 20–28%. This further demonstrates that the

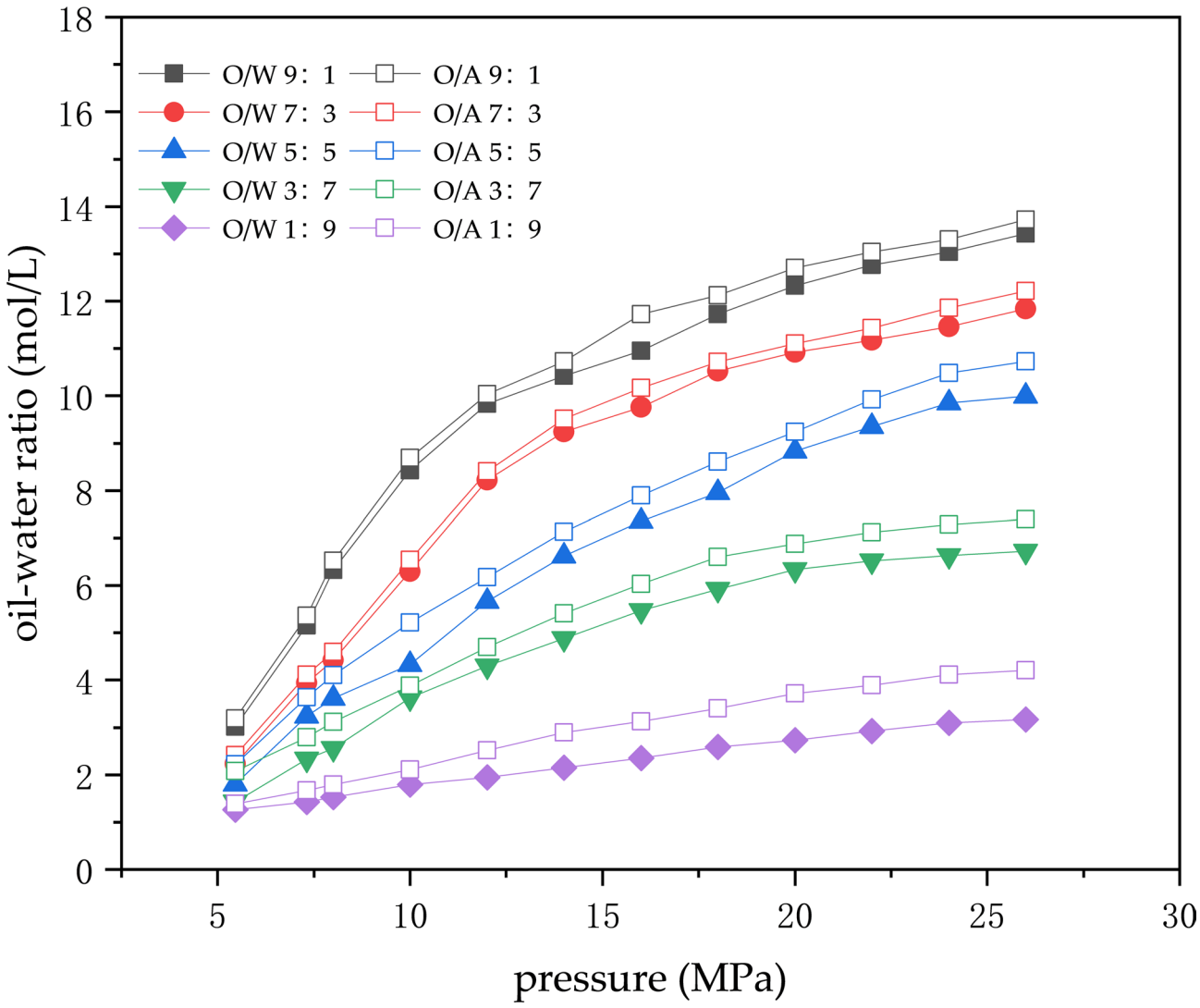

Fig. 3. Solubility comparison of mixed fluids (O/W and O/A denote the oil-water and oil-agent ratios, respectively).

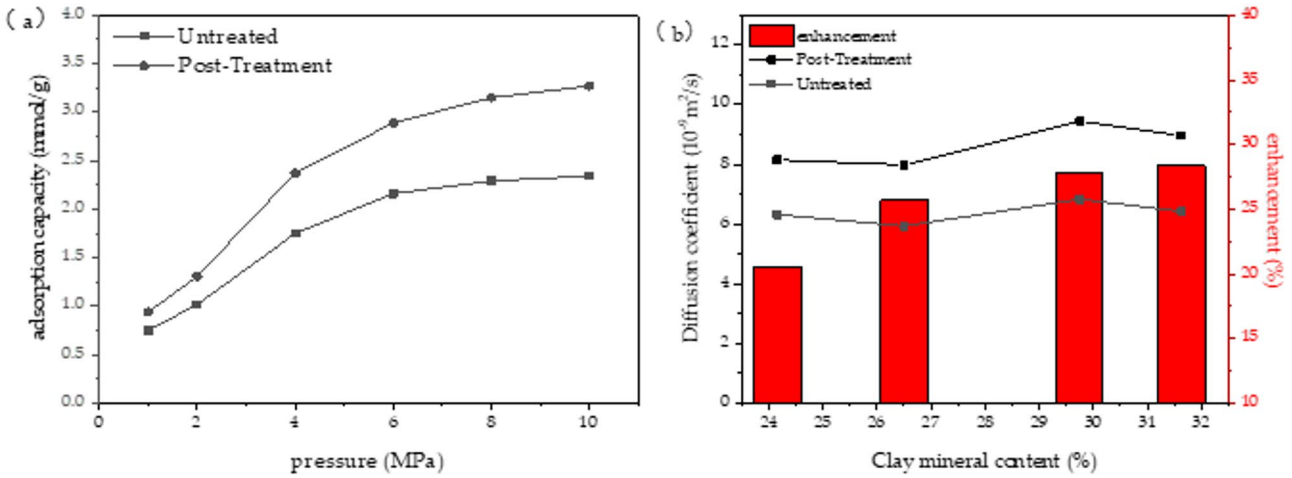

Fig. 4. Properties of core samples before and after treatment. (**a**) Adsorption capacity. (**b**) Diffusion coefficient.

Core type	Total clay content	Relative clay content				Average permeability (K)	Average porosity (Φ)	Oil saturation (S_o)	Effective Diffusion coefficient(D_{eff})
		K	I	M	O				
	%	%	%	%	%	$\times10^{-3}\mu m^2$	%	%	$10^{-9}m^2/s$
Artificial core	0	0	0	0	0	10.23	15.82	50.62	17.032
Berea Sandstone Core	13.72	52.32	36.7	5.62	5.36	9.85	14.59	52.29	11.463
	12.16	57.68	31.15	8.34	2.83	8.69	15.72	48.60	10.915
Natural core	25.36	28.58	9.52	60.37	1.53	10.51	15.16	50.16	9.226
	32.94	34.26	6.8	57.15	1.79	10.93	14.27	51.22	8.376

Table 6. CO_2 dissolution coefficients in cores with different clay content. *K(Kaolinite), I(Illite), M(Montmorillonite), O(Other).

presence of clay restricts the diffusion properties of CO_2 in pores, a phenomenon attributed to pore structure modification and subsequent CO_2 adsorption.

As demonstrated in Table 6, the diffusion capability of CO_2 is found to decrease with an increase in clay mineral content. The diffusion coefficient of CO_2 in the man-made core is determined to be $17.032\times10^{-9}m^2/s$, with no alteration in the pore structure and no adsorption of CO_2 by the clay. Conversely, the clay mineral content of the Berea sandstone core and the natural core exhibited an increase to 13.72% and 25.36%, respectively. The diffusion coefficients were found to be $11.463\times10^{-9}m^2/s$ and $9.226\times10^{-9}m^2/s$, attributed primarily to alterations in the pore structure and the adsorption of CO_2 by the clay. The values of $11.463\times10^{-9}m^2/s$ and $9.226\times10^{-9}m^2/s$ are attributed to the increase in clay mineral content, which is dominated by kaolinite (57.68%) and illite (31.15%) in the Berea sandstone core. The natural cores in the study area are dominated by montmorillonite (60.37%) and kaolinite (28.58%). Notably, these measurements were conducted under equilibrated oil-water saturations (50.16–52.29% oil), where CO_2 exhibited a higher solubility in oil (6.346 mol/L) than in water (0.875 mol/L), as depicted in Fig. 2. This solubility disparity established a concentration gradient favorable for diffusion through oil-wet pores. At 50% oil saturation, the oil phase served as the primary CO_2 transport pathway, with the diffusion coefficient an order of magnitude higher than that under water-wet conditions (Fig. 5).

Injection pressure

The first set of experiments investigated the variation law of diffusion coefficient at different pressures (5.61 ~ 27.53 MPa), as shown in Fig. 6. The PSC was used as the boundary to divide the pressure into gaseous and supercritical states. Two conclusions were drawn from the experimental results: (1) the diffusion coefficient increased rapidly from 2.152 ($\times10^{-9}m^2/s$) to 6.497 ($\times10^{-9}m^2/s$) when increasing from saturation pressure (the first set of data) to critical pressure (the second set of data). This phenomenon can be explained by the change of CO_2 phase state, when the saturation pressure when the CO_2 is gaseous, pressurisation to the phase transition pressure when the transition to the supercritical state, so when the CO_2 injection pressure increases, the density of CO_2 molecules increases, which leads to an increase in the diffusion of the mass of the gas, the gas solubility of the stratum fluid to improve. (2) The growth rate of the CO_2 diffusion coefficient gradually slows down when the pressure continues to rise. This is because the amount of dissolved CO_2 in the reservoir fluid tends to be saturated, resulting in a slowdown in the growth rate[49].

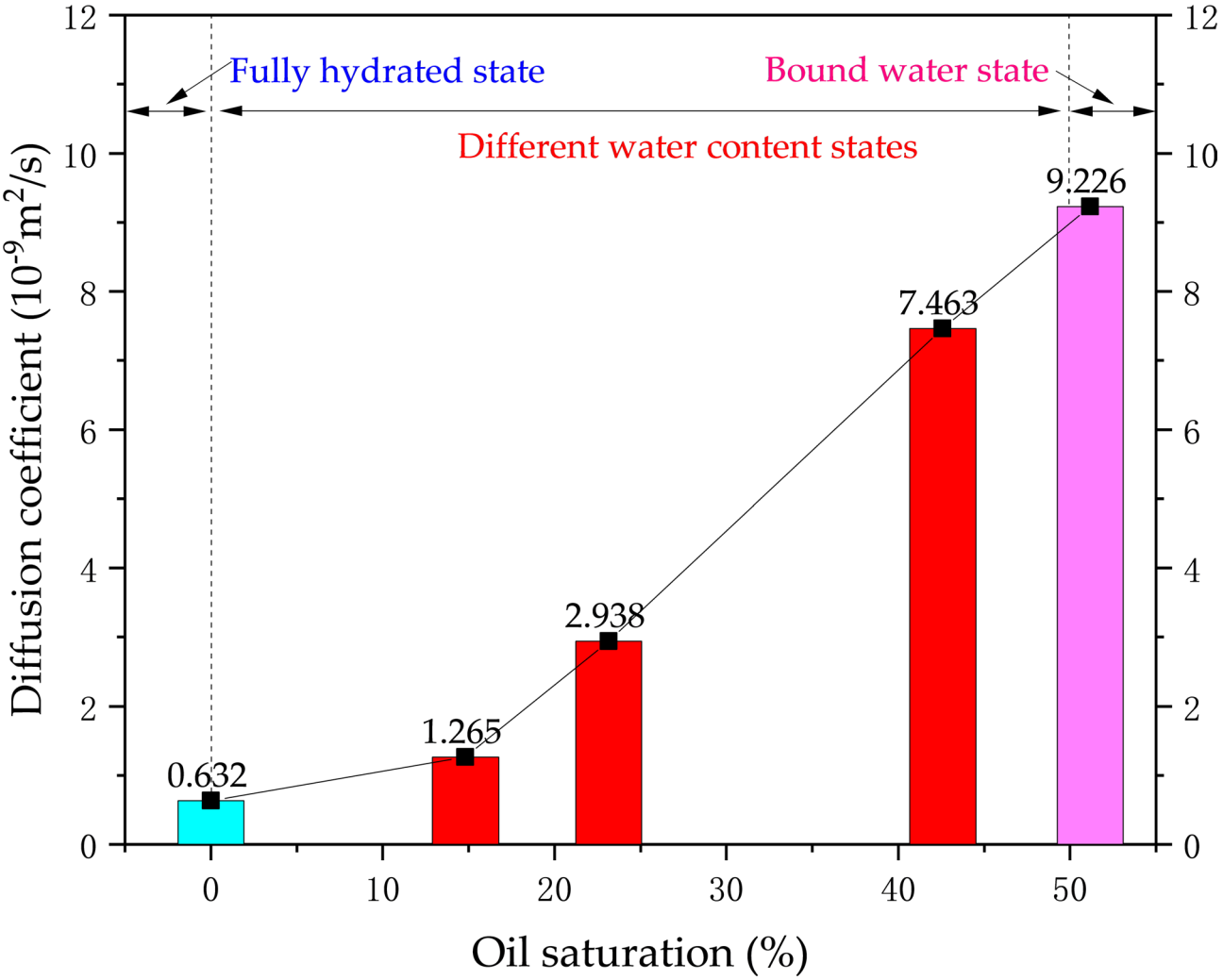

Fig. 5. Dissolved CO_2 diffusion coefficients at different oil saturations.

Oil saturation

Two results can be summarised from Fig. 5: (1) The diffusion coefficient of CO_2 in porous media increases significantly with the increase of oil saturation. Oil saturation is achieved by fixing the injection rate and implementing simultaneous injection with different oil-water ratios[50]. Since crude oil is a mixture of various liquid hydrocarbons such as alkanes, naphthenes, aromatic hydrocarbons, and olefins, the solubility of supercritical CO_2 in crude oil is much higher than that in brine. Therefore, the diffusion coefficients in the cores in the oil-bearing state are all one order of magnitude higher than those in the non-oil-bearing cores. (2) Different oil content in porous media corresponds to different stages of reservoir water injection development. The CO_2 dissolution is extremely small when the water is completely contained. With the increasing oil/water ratio, the content of CO_2 dissolved in crude oil continues to increase. In the bound water state, the crude oil content in the porous medium reaches the maximum, and the crude oil mainly exists in the large pores. The interaction space with CO_2 reaches the limit, and the gas diffusion coefficient reaches the maximum.

Permeability

From Fig. 7, it can be observed that the diffusion coefficient of CO_2 in the porous medium continues to grow with the increase of the permeability of the core. The diffusion coefficient grows rapidly from type 1 (extra-low permeability core TypeI, 5-10mD) to type 2 (low permeability core TypeII, 10–100 mD). The growth trend of diffusion coefficient continues to type3 (medium permeability core typeIII>100mD) is gradually stabilised. The reason for this is that with the increase of permeability, the pore distribution of the cores gradually becomes larger, and the tortuosity factor decreases significantly, which makes supercritical CO_2 easier to be transported in the porous medium.

Development of mathematical models for CO_2 diffusion coefficient

The assumptions made on the mathematical model are as follows. (1) capillary forces and gravity are not considered; (2) the fluid is incompressible during the flow; (3) the cores used for the experiment are homogeneous

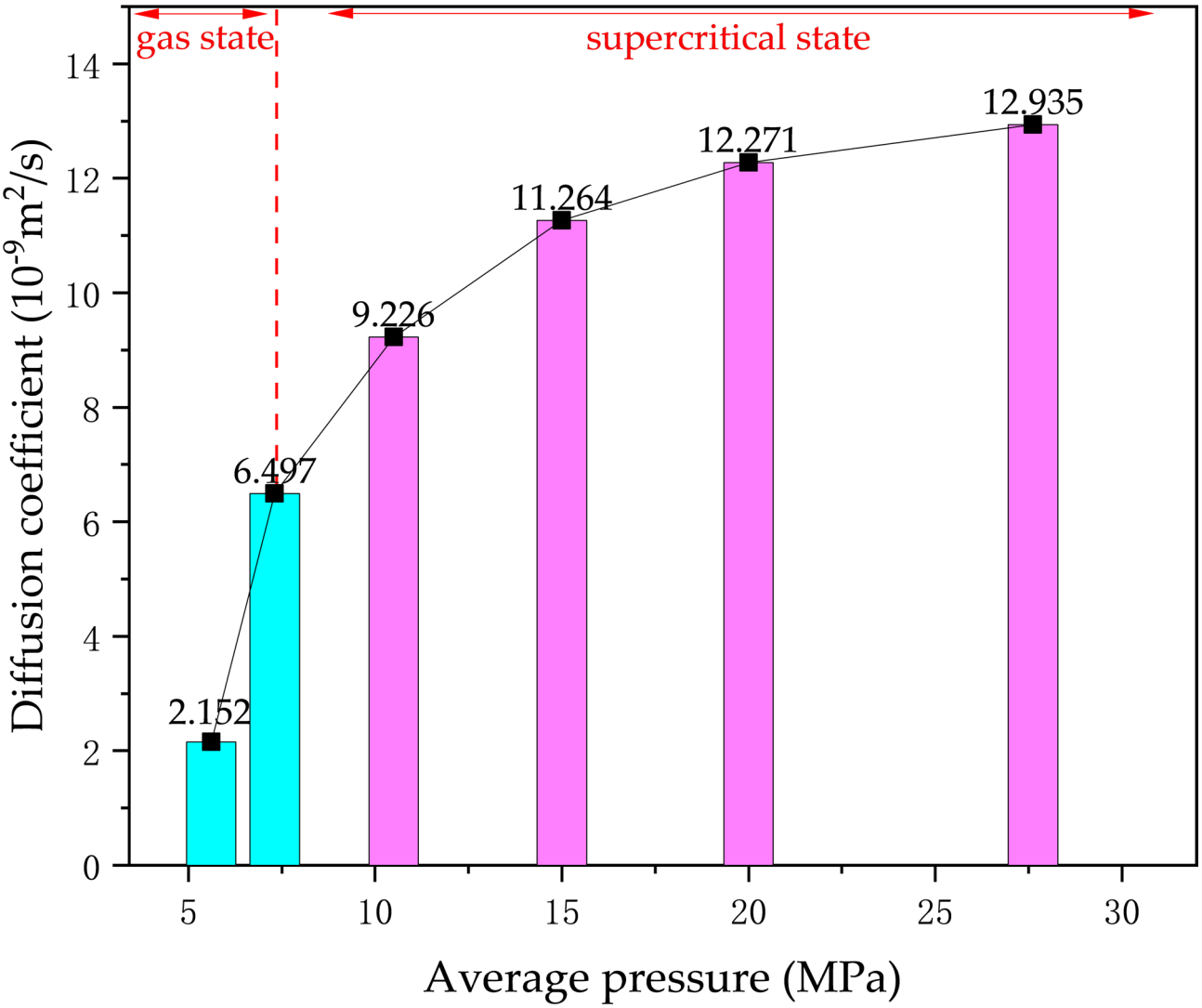

Fig. 6. Dissolved diffusion coefficient of CO_2 at different pressures.

and isotropic, with oil and water uniformly distributed in the cores; (4) the diffusion coefficient of CO_2 in the cores is constant during measurements; (5) the concentration of CO_2 in the liquid phase is constant during measurements; (6) natural convection due to the difference in fluid density is neglected; ((7) Evaporation from the liquid phase to the gas phase is neglected; (8) Immiscibility of the oil and liquid phases during the measurement.

Based on the above assumptions, a mathematical description of CO_2 diffusion in the physical model under non-expansive conditions can be obtained from Fick's first law and the continuity Eqs. 5[1,53], as shown in Eq. 1.

$$\frac{\partial c}{\partial t} = D_{\text{eff}} \times \frac{1}{r} \times \frac{\partial}{\partial r}\left(r\frac{\partial c}{\partial r}\right) \tag{1}$$

At the instant when CO_2 injection begins, the gas phase does not immediately dissolve into the liquid phase, so the initial conditions for the diffusion process are shown in Eq. (2).

$$\mathrm{C}\ (r,t)\,|_{t=0} = 0, (0 < r < r_0) \tag{2}$$

The boundary constraints are shown in Eq. 3.

$$D\frac{\partial C}{\partial r}|_{r=r_0} = K\left[C_{eq} - \mathrm{C}\ (r,t)\,|_{r=r_0}\right], \mathrm{t} \geq 0 \tag{3}$$

Where Ceq is the CO_2 concentration at the equilibrium pressure Peq; K is the mass transfer coefficient at the gas-liquid interface, which is also the resistance to mass transfer at the gas-liquid interface.

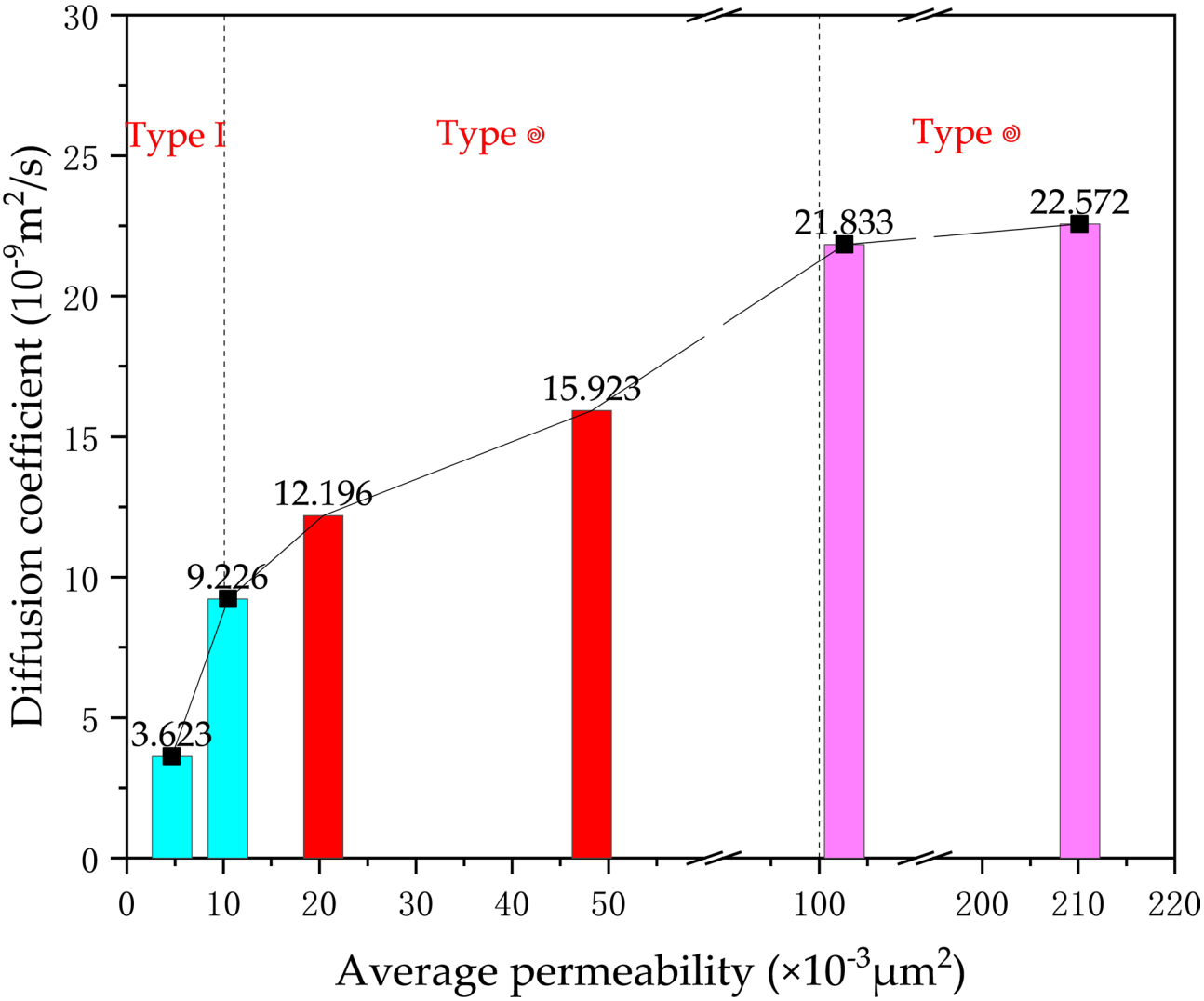

Fig. 7. Dissolved CO_2 diffusion coefficients of cores with different permeabilities.

By introducing the time $\tau = t/(D_{eff}/r_0)$, the length $\bar{r} = r/r_0$ the velocity $\bar{u} = u/(D_{eff}/r_0)$, and the concentration $\bar{c} = (c - c_i)/(c_0 - c_i)$. The partition coefficients for the concentration of CO_2 in the oil and water phases are expressed as k_{pco} and k_{pcw}. A new set of dimensionless variables is defined.

$$\partial \frac{\bar{c}}{\partial \tau} + k_{pco} \times \bar{c}\, \partial \frac{\bar{c}}{\partial \bar{r}} + k_{pco} \times \frac{\bar{c}\bar{u}}{\bar{r}} + k_{pcw} \times \bar{c}\, \partial \frac{\bar{c}}{\partial \bar{r}} + k_{pcw} \times \frac{\bar{c}\bar{u}}{\bar{r}} + \lambda\, \partial \frac{\bar{c}}{\partial \bar{r}} = \frac{\partial^2 \bar{c}}{\partial \bar{r}^2} \tag{4}$$

The boundary conditions simplify to Eq. 5.

$$\begin{cases} \bar{u} = 0, \partial \frac{\bar{u}}{\partial \bar{r}} = 0, \left(\tau > 0, \bar{r} = 0\right) \\ \bar{c} = 1, \left(\bar{r} = 1, \tau > 0\right) \end{cases} \tag{5}$$

The initial conditions simplify to Eq. 6.

$$\begin{cases} \bar{u} = 0, \bar{c} = 0, \left(\tau = 0, \bar{r} < 1\right) \\ \bar{u} = 0, \bar{c} = 1, \left(\tau = 0, \bar{r} = 1\right) \end{cases} \tag{6}$$

In this study, the fully implicit finite difference method is used in the solution process. The differential equations are discretised into a system of difference equations and solved iteratively. In the discretisation process, the

first and second order derivatives of concentration and velocity concerning displacement are in centre difference format; the first order derivatives of time are in forward difference format. The concentration and velocity distributions were calculated for each time step by the continuous displacement method. The iterative calculations were repeated until the maximum relative error was less than the error tolerance of 10^{-4} set in this study.

$$a_i \bar{c}_{i-1}^{n+1} + b_i \bar{c}_i^{n+1} + e_i \cdot \bar{c}_{i+1}^{n+1} = \bar{c}_i^{n}, (i = 0,1,2,3 \ldots, I) \tag{7}$$

Where the parameters are shown in Eq. 8.

$$\begin{cases} a_i = -\frac{\Delta \tau}{\Delta \bar{r}^2} - \frac{\Delta \tau}{2\Delta \bar{r}} \bar{u}_i^{n+1} \\ b_i = 1 + \frac{2\Delta \tau}{\Delta \bar{r}^2} + \frac{\Delta \tau}{2\Delta \bar{r}} \left(\bar{u}_{i+1}^{n+1} - \bar{u}_{i-1}^{n+1} \right) \\ e_i = -\frac{\Delta \tau}{\Delta \bar{r}^2} + \frac{\Delta \tau}{2\Delta \bar{r}} \times \bar{u}_i^{n+1} \end{cases} \tag{8}$$

Once the CO_2 concentration field is determined, the velocity field equation can be solved.

$$\bar{u}_{i+1}^{n+1} = \frac{\bar{r}_i \cdot \Delta \bar{r}}{(\bar{r}_i + \Delta \bar{r}) \cdot \Delta \tau} F(c) c_0 \varnothing \times \frac{\left(c_{i+1}^{n+1} + c_i^{n+1}\right) - \left(c_{i+1}^{n} + c_i^{n}\right)}{2} \tag{9}$$

Starting from the real gas equation of state and the law of mass conservation, the gas amount lost in the gas phase of the diffusing component and the gas amount entering the liquid phase were determined. The true gas state equation is shown in Eq. 10.

$$\mathrm{PV} = \mathrm{nRT} \tag{10}$$

Where p denotes the gas pressure, V the gas volume, n the amount of substance, T the temperature, and R the gas constant.

The amount of CO_2 reduced in the Gas Phase, Δn_t is obtained by calculating the equation of state of the gas to get the amount of CO_2 reduced in the Gas Phase from the initial state of the real gas to a given time in the state (p_t, t_i), which gives Eq. 11.

$$\Delta n_g = n_o - n_t = \frac{1}{RT}\left(\frac{P_o V_o}{Z_o} - \frac{p_t V_t}{Z_t}\right) = \frac{\Delta P_o V}{ZRT} \tag{11}$$

From the law of conservation of mass and the real gas equation of state, the reduction of CO_2 in the gas phase is equal to the diffusive flux through the interface, which gives Eq. (11).

$$\Delta P = \frac{qZRT - \Delta V P_o}{V - \Delta V} \tag{12}$$

Where Z is the gas deviation factor, R is the gas constant, T is the absolute temperature, P_o is the initial pressure of the gas before diffusion, ΔV is the volume reduction of the gas phase, and q is the amount of gas lost in the gas phase at time t. Notably, q was obtained by deriving the pressure-time relationship through the pressure decay method, followed by calculation via the gas state equation (Eq. 10).

The diffusion coefficient (D) was extracted from pressure decay data using a modified Fick's second law approach, combining real gas behavior and mass conservation principles.

The rate of CO_2 loss from the gas phase equals the diffusive flux through the interface.

$$\frac{d_{ng}}{dt} = -D \cdot A \cdot \frac{d_c}{d_r}|_{r=r_0} \tag{13}$$

Where A = πr2 is the interface area, r0 is the core radius, and $\frac{\mathrm{d_c}}{\mathrm{d_r}}|_{\mathrm{r=r_0}}$ is the concentration gradient at the interface.

Assuming equilibrium at the interface, the concentration gradient is approximated as Eq. 14.

$$\frac{\mathrm{d_c}}{\mathrm{d_r}}|_{\mathrm{r=r_0}} \approx \frac{\mathrm{C_{eq}} - \mathrm{c_0}}{\mathrm{r_0}} \tag{14}$$

where Ceq is the equilibrium CO_2 concentration (mol/m³) at pressureP(t), and C0 is the initial concentration in the liquid phase.

Substitution and simplification yield the final diffusion coefficient equation as shown in Eq. 15.

$$\mathrm{D} = \frac{\mathrm{RTr_0}}{\mathrm{V_g P_0}} \cdot \frac{\mathrm{d_P}}{\mathrm{dt}} \cdot \frac{1}{\mathrm{C_{eq}} - \mathrm{c_0}} \tag{15}$$

Where D is the diffusion coefficient, P0 is the initial pressure, $\frac{dP}{dt}$ is obtained by fitting the pressure decay curve with a first-order exponential function.

The simulation was conducted using custom code and validated by comparison with CMG software, with the prediction deviation of the diffusion coefficient being less than 5%. 11 is used to match the experimentally measured pressure drop ΔP_{Exp} and $t_{1/2}$ curve to determine the diffusion coefficient of CO_2 in the oil-water coexistence state in the porous medium. The base physical properties of formation water and injection water in the low-permeability strong water-sensitive rock reservoir studied in this paper are quite different, so the oil-phase and liquid-phase partition coefficients are introduced during the mathematical model solving process to consider the difference of dissolution and diffusion when the two-phase fluids coexist, which is closer to the actual situation. Based on the double-constant cubic equation of state, the interaction of the material system and the phase equilibrium is taken into account, improving the diffusion coefficient's calculation accuracy.

This numerical model introduces three new technologies, addressing key issues in traditional single-phase diffusion models and validated by experimental data (Table 6; Fig. 8).

1. Two-phase partition coefficient framework: For the first time, oil-water partition coefficients were integrated to describe CO_2 mass transfer between phases, a critical oversight in previous studies. These coefficients quantify CO_2 dissolution partitioning under oil-water coexistence and were derived from PVT experiments (Fig. 2), showing that CO_2 solubility in oil is 7.25 times higher than in water. Thus, the model accurately predicts multiphase diffusion in water-sensitive reservoirs, aligning more closely with actual reservoir conditions compared to single-phase models.
2. Clay adsorption correction term: A clay-CO_2 adsorption term was added to Fick's law (Eq. 4) to account for the high adsorption capacity of montmorillonite, capturing CO_2 retention on clay surfaces. The model predicts diffusion coefficients with 92% accuracy compared to experiments (Fig. 8), a 15% improvement over models ignoring adsorption.

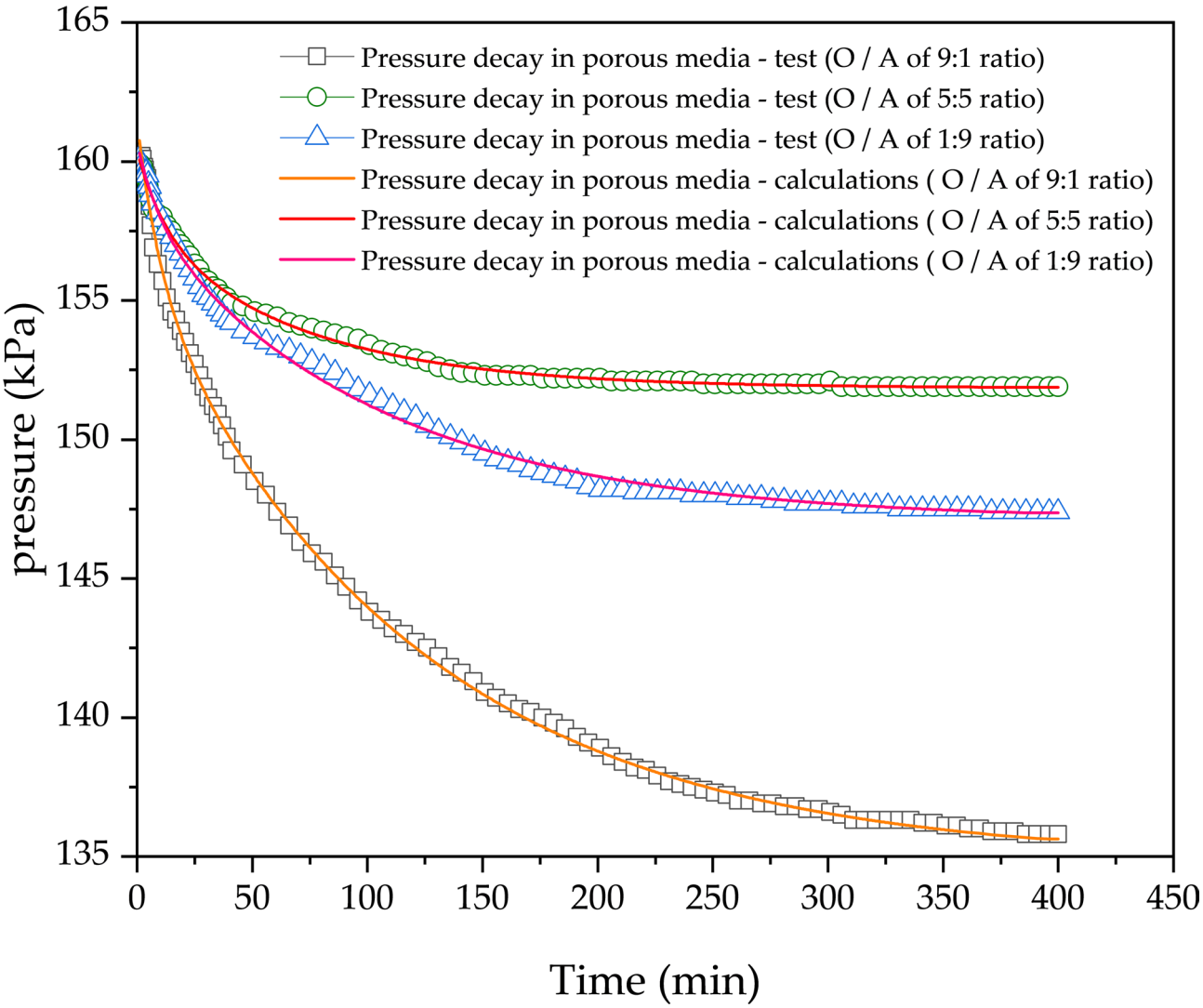

Fig. 8. Experimental and computational numerical fitting.

Synergistic effects of enhanced recovery and carbon sequestration potential

Microscopic visualisation studies

Through visualized microscopic oil displacement experiments in glass micromodels, we systematically analyzed displacement mechanisms and remaining oil distribution under reservoir conditions (42 °C, 15 MPa). The microdynamic mechanisms of the anti-swelling system/CO_2 flooding were elucidated, and the characteristics of remaining oil distribution under original reservoir conditions were quantified. Quantitative analysis results of residual oil morphology are shown in Fig. 9. Two conclusions can be drawn from the experimental results: firstly, the sweep efficiency of the CO_2 flooding (42.19%) is much smaller than that of the anti-swelling system/CO_2 flooding (73.95%). The reason is that CO_2 has a faster breakthrough rate in the pore space, CO_2 mainly exists in a continuous form, and the fluid flushing area shows a block division phenomenon, which has a poorer oil washing effect. The flow resistance formed by the anti-swelling system/CO_2 flooding slows down the CO_2 advancement, so that the subsequent CO_2 entering the pore space is diverted to enter the small pore space that has not been reached, thus enlarging the area of reach and prolonging the interaction time with the crude oil, as shown in Fig. 10.

Secondly, the ratio columns of five different forms of residual oil (Oil-droplet, Columnar, Membranous, Blind-end, and Clustered) were quantified. It was found that the area of clustered residual oil decreased by 78%, the most significant reduction among all types; columnar, film-like, and blind-end oils decreased by 45–65%, while droplet-shaped oil remained relatively unchanged. This demonstrates that the dual-medium system balances capillary trapping (via anti-swelling agents) and viscosity reduction (via CO_2 dissolution), achieving dual effects of expanding sweep efficiency and enhancing oil displacement efficiency. This synergistic effect increased oil recovery efficiency by 23.61%, with results consistent with core flooding data (Fig. 11(b)).

Enhanced oil recovery and carbon sequestration potential

By analyzing the dynamic performance of different injection strategies (continuous CO_2, water-alternating-gas (WAG), and anti-swelling system-alternating-gas (ASAG)) as shown in Fig. 11, the synergistic mechanisms of CO_2 sequestration and oil recovery were elucidated with explicit mechanistic insights:

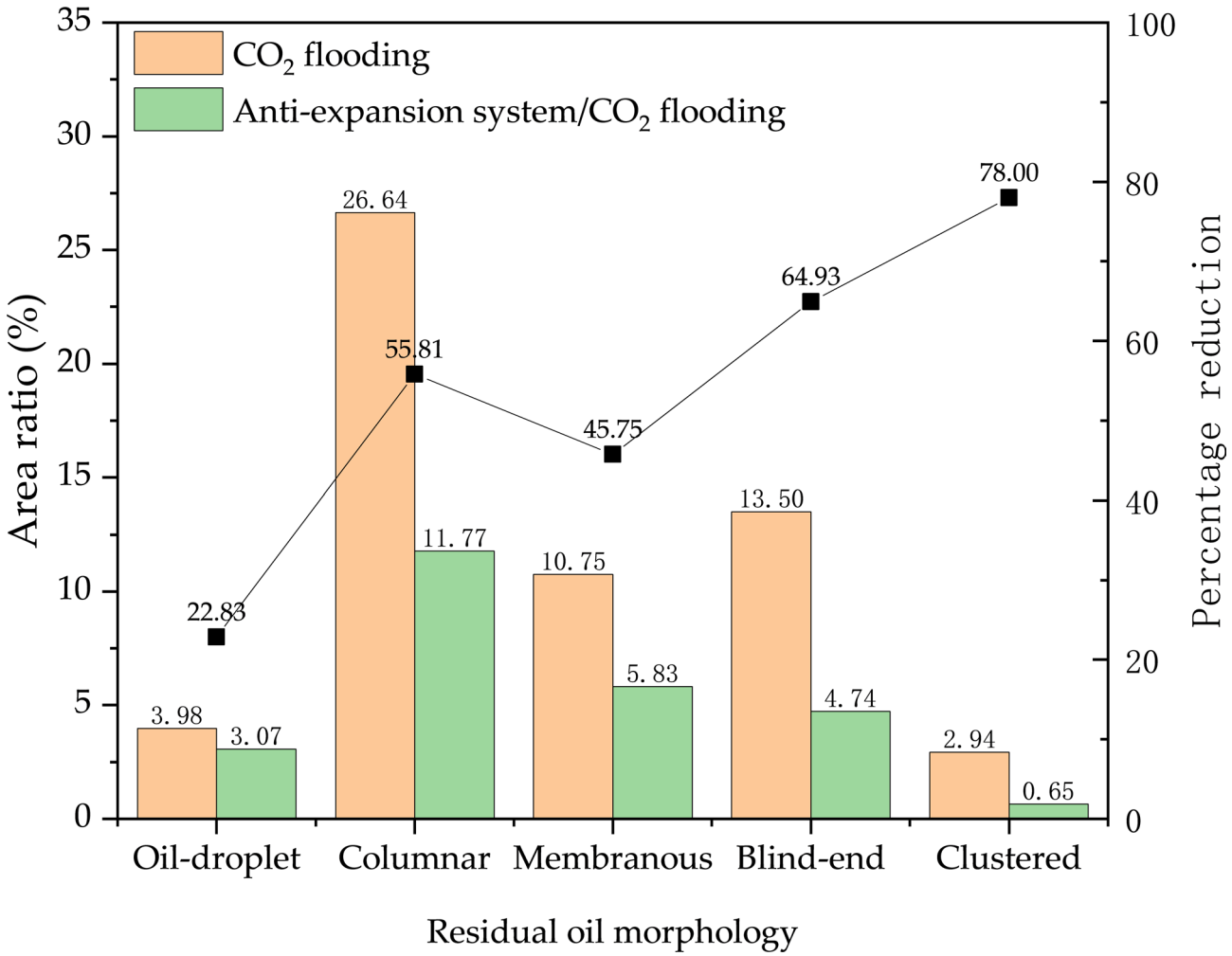

Fig. 9. Residual oils of different types.

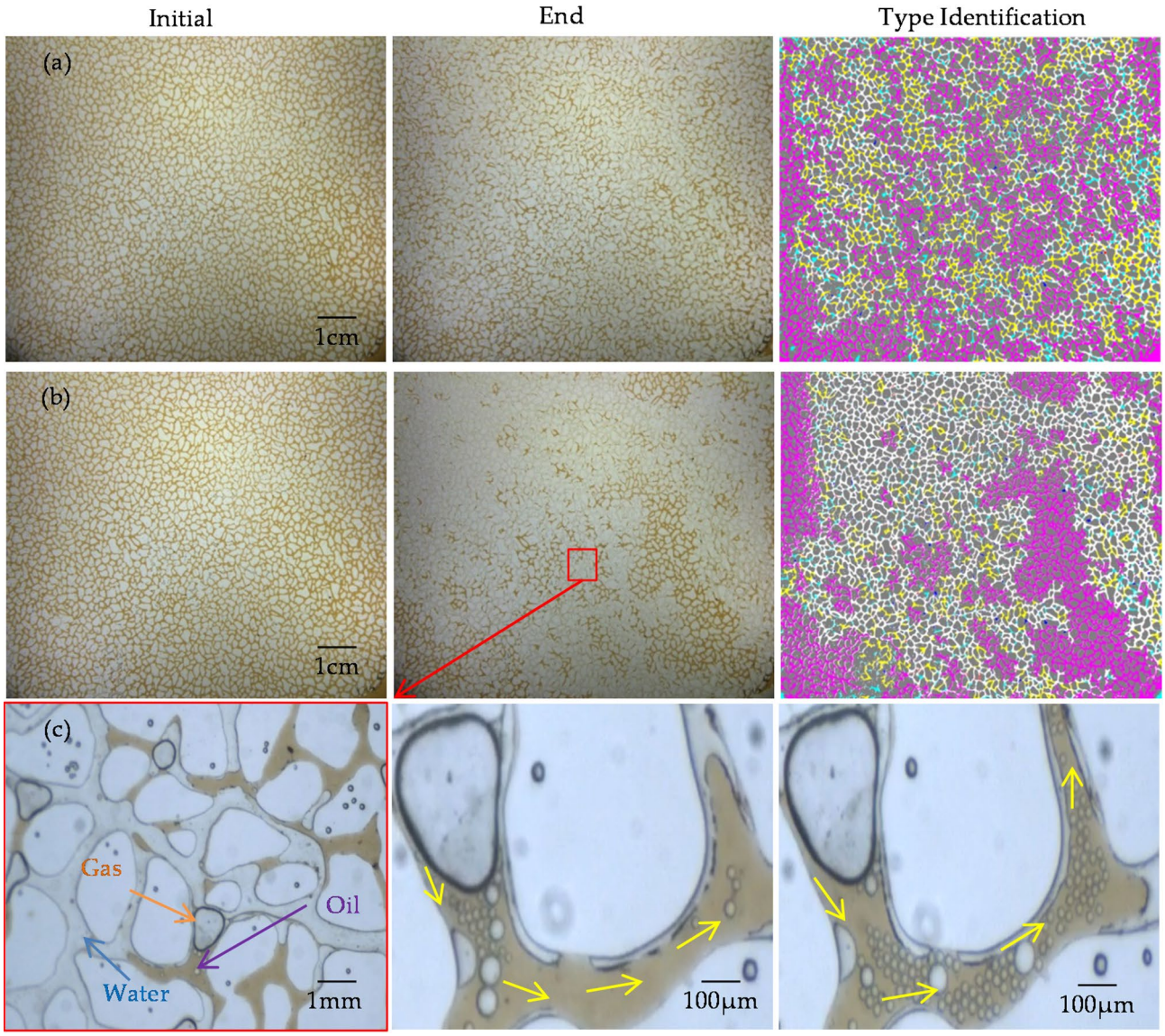

Fig. 10. Micro-visualisation of flooding. (**a**) CO_2 flooding. (**b**) Anti-swelling system/CO_2 alternating flooding.

1. CO_2 Sequestration-EOR Trade-off Analysis.

Continuous CO_2 injection achieved the highest sequestration efficiency (49.70%) but only 35.64% oil recovery, attributed to rapid gas breakthrough (Fig. 11a-b). In contrast, ASAG injection increased oil recovery to 58.12% with a marginal 3.54% reduction in sequestration efficiency (46.16%). This synergy arises from two mechanisms: The anti-swelling system inhibited 94.09% of clay swelling, maintaining pore connectivity and enhancing CO_2 diffusion by 20–28% (Table 4). This enabled deeper CO_2 penetration into fine pores, releasing clustered residual oil (78% reduction in clustered oil area, Fig. 9). Additionally, alternating injection prolonged CO_2-rock contact time by 0.17 PV, increasing in-situ CO_2 dissolution in oil and promoting viscosity reduction, thereby improving sweep efficiency (73.95% vs. 42.19% for continuous CO_2, Fig. 10).

2. Pressure Dynamics and Seepage Mechanisms.

Water flooding induced 19.3% higher injection pressure than ASAG due to clay lattice expansion narrowing pore throats. The ASAG system mitigated this via multicomponent synergism of the anti-swelling system: clay inhibitors neutralized surface negative charges through cation adsorption, inorganic salts compressed the double electric layer via ionic strength, non-ionic surfactants improved wettability, and ethylene glycol reduced water activity through hydrogen bonding to decrease water penetration drive. Additionally, dissolved CO_2 enhanced oil mobility by lowering viscosity, enabling better displacement of residual oil in micro-throats.

3. Gas-Oil Ratio (GOR) Evolution.

ASAG injection delayed CO_2 breakthrough by 0.17 PV compared to continuous CO_2 (Fig. 11d), indicating more uniform CO_2 distribution. Full-cycle saturation maps (Fig. 12) confirmed 15–20% higher CO_2 saturation at the production end for ASAG, reflecting improved sweep uniformity in clay-rich zones.

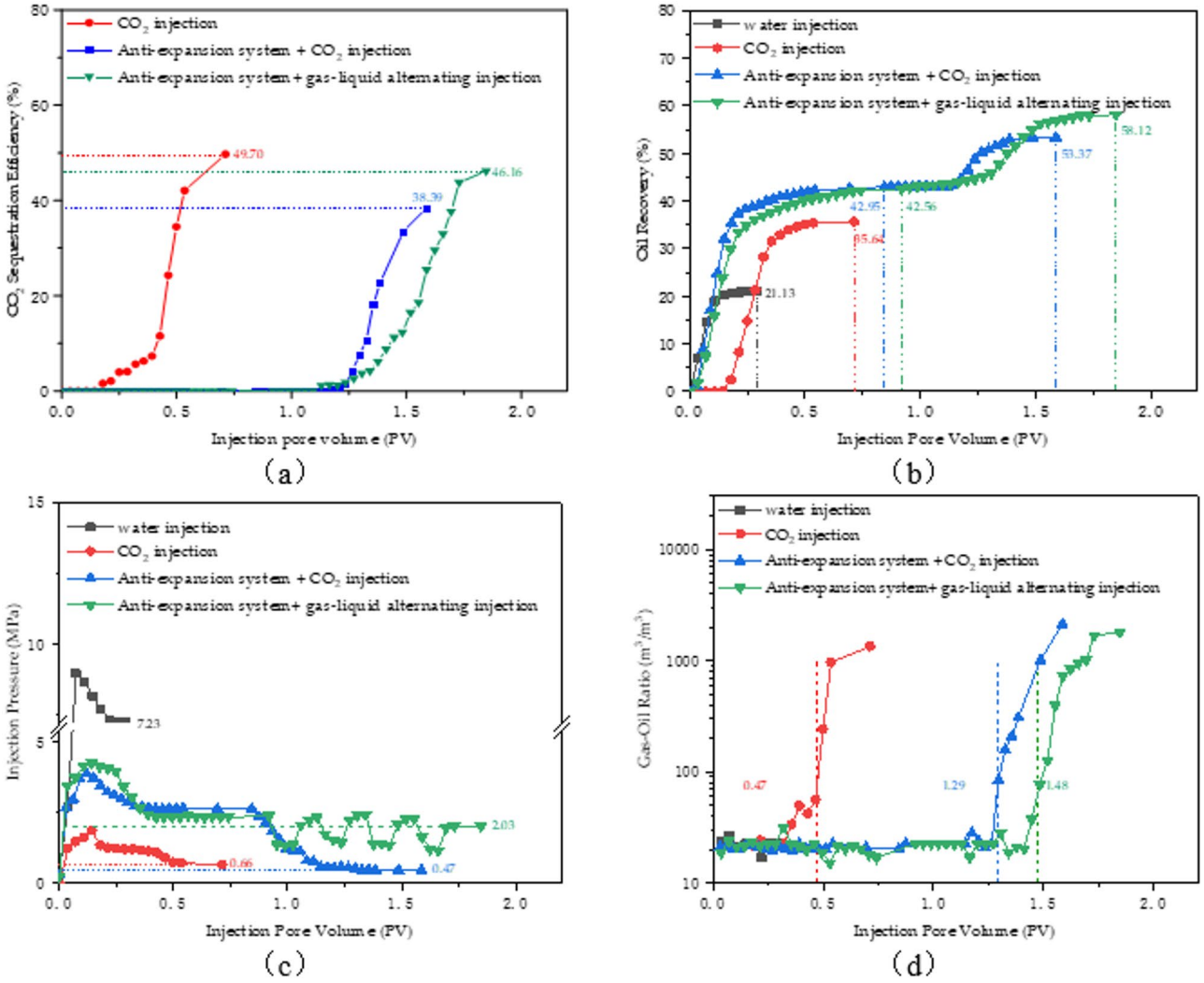

Fig. 11. Production performance curves of different injection patterns (**a**) Relationship between CO_2 sequestration efficiency and injection patterns (**b**) Relationship between oil recovery efficiency and injection patterns (**c**) Dynamic variation law of injection pressure differential (**d**) Dynamic variation curve of gas-oil ratio (GOR).

These findings demonstrate that the ASAG strategy achieves efficient coupling of sequestration and recovery through a "dual-stabilization" mechanism: anti-swelling agents maintain pore accessibility, while CO_2 dissolution optimizes oil mobility. This addresses the core challenge of water-sensitive reservoirs, where conventional methods cannot balance sequestration and recovery.

Full-cycle CO2 saturation changes

As shown in Fig. 12, the carbon sequestration potential of different reservoir properties is compared, the evolution process of full-cycle CO_2 saturation is clarified, and the change rule of CO_2 sequestration efficiency with time and space is quantified. The following two conclusions are drawn, (1) the CO_2 content of the cores with three permeabilities at the same injection stage shows a decreasing trend from the injection end to the withdrawal end, which is due to the highest injection pressure at the injection end, which has a stronger ability to enter the pore throat and interact with the crude oil, and with the advancement of the driving leading edge to the withdrawal end, the injection pressure decreases, resulting in a weakening of the ability of the CO_2 to displace the fluid in the pore space. (2) Taking the third cycle of alternating injection as an example, the CO_2 sequestration efficiency (68.3%, 59.2%, and 42.5%) of 10.15, 42.71, and 102.75×10^{-3} μm^2 cores at 2/5 distance were compared, and it was concluded that there is an increasing trend in the CO_2 sequestration efficiency with increasing permeability. The reason is that with the increase of permeability, the pore throat size also increases, the reaction space between CO_2 and formation fluid relatively increases, and the replacement capacity improves, so the CO_2 sequestration efficiency shows an upward trend.

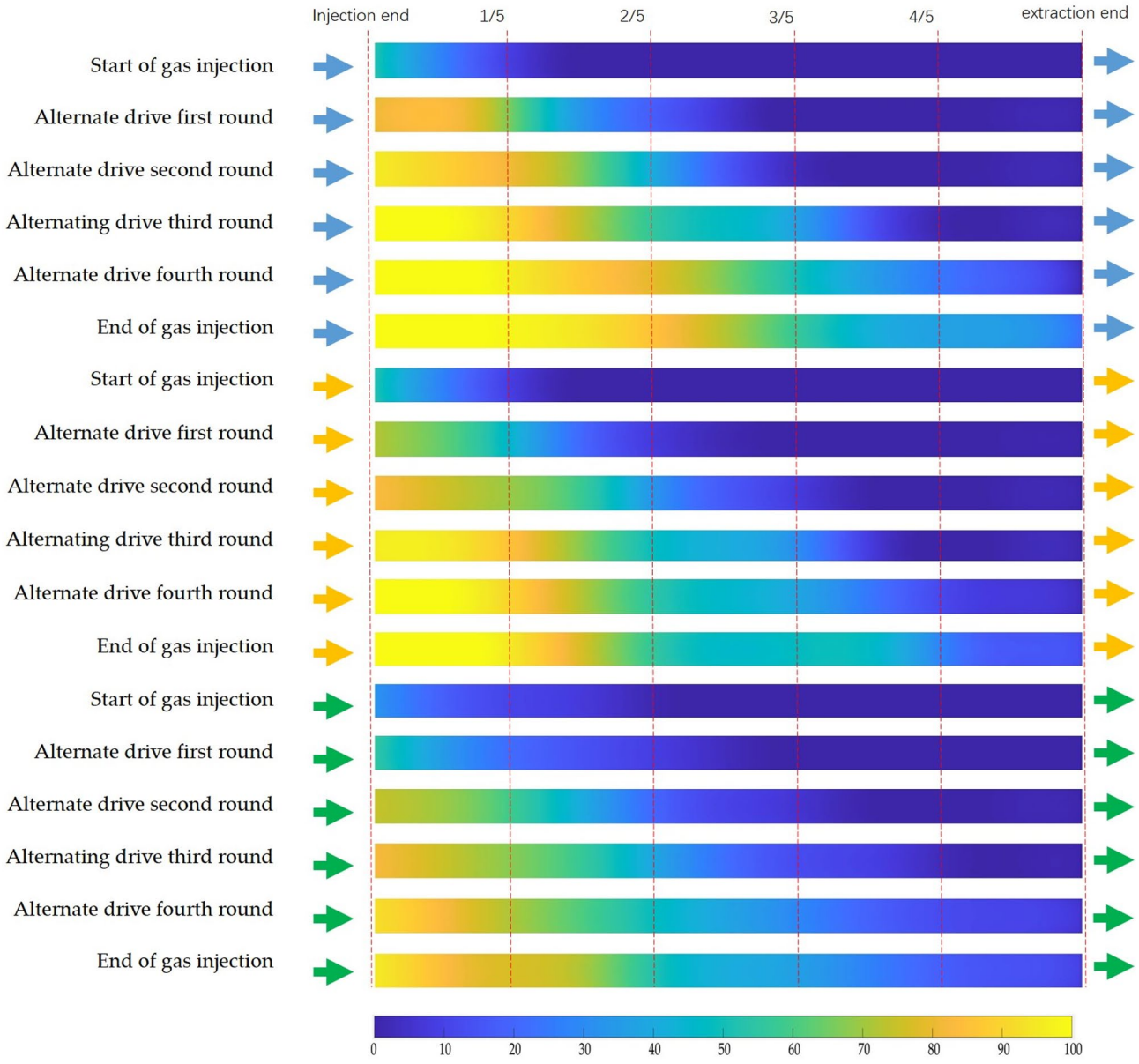

Fig. 12. Variation of CO_2 concentration along the course of cores with different (Permeabilities of 102.75, 42.71, and 10.15×10^{-3} μm^2 are labelled with blue, yellow, and green arrows).

Conclusions

(1)Supercritical CO_2 diffusion experiments reveal a "surge-decelerate" trend in diffusion coefficients with increasing clay content, pressure, oil saturation, and permeability, directly evidencing the inhibitory effect of high clay concentrations on CO_2 transport.

(2)The improved model, integrating oil-water coexistence thermodynamics and clay-inhibited dissolution coefficients with PR-EOS phase behavior, demonstrates > 92% agreement with experimental data. This framework enhances prediction accuracy by 15% relative to traditional single-liquid phase models, addressing critical limitations in clay-dominated low-permeability systems.

(3)Combined microscopic visualization and macroscopic core flooding experiments confirm that the "anti-swelling system-CO_2 alternating injection" strategy improves sweep efficiency substantially, achieving 58.12% oil recovery and a 46.16% CO_2 sequestration efficiency. Contour plots visualize dynamic CO_2 saturation evolution, highlighting the technology's dual benefit for enhanced oil recovery and subsurface CO_2 storage.

The technology works synergistically through a 'dual flow stabilisation mechanism' - an anti-swelling system to stabilise pore throat narrowing and CO_2 dissolution to reduce crude oil viscosity. The study quantified for the first time the synergistic effect of 'sand-fixing-viscosity-reducing-sequestration' in a strong water-sensitive reservoir, confirmed its technical feasibility as a CO_2 sequestration site, and provided a comprehensive solution for the development of the same type of low-carbon reservoir.

In terms of practical application, this technology has been implemented in field pilot tests for water-sensitive reservoirs. Compared with conventional CO_2 flooding processes, it has achieved a reduction in injection pressure and an extension of CO_2 breakthrough time. Future research will focus on three aspects: (1) optimizing adaptability to reservoirs with different permeability gradients; (2) improving well pattern deployment and injection parameter design through numerical simulation; (3) conducting long-term storage safety monitoring, to provide a field-verified technical solution framework for the large-scale development of similar low-carbon reservoirs.

Data availability

Restrictions apply to the datasets. The datasets presented in this paper are not readily available because the research fund project is in the ongoing research phase, and the data are part of the ongoing research. Requests to access the datasets should be directed to sygc8810@163.com.

Received: 13 May 2025; Accepted: 14 July 2025
Published online: 26 July 2025

References

1. Jiang, S. et al. A state-of-the-art review of CO2 enhanced oil recovery as a promising technology to achieve carbon neutrality in China. *Environ. Res.* **210**, 112986 (2022).
2. Fareed, A. G. et al. Underground geological sequestration of carbon dioxide (CO2) and its effect on possible enhanced gas and oil recovery in a fractured reservoir of Eastern Potwar basin, Pakistan. *Sci. Total Environ.* **905**, 167124 (2023).
3. El-kaseeh, G., Will, R., Balch, R. & Grigg, R. Multi-scale seismic measurements for CO2 monitoring in an EOR/CCUS project. *Energy Procedia*. **114**, 3656–3670 (2017).
4. Zhao, L. et al. Research on the timing of WAG intervention in low permeability reservoir CO2 flooding process to improve CO2 performance and enhance recovery. *Energies* **16**, 7373 (2023).
5. Kumar Pandey, R., Gandomkar, A., Vaferi, B., Kumar, A. & Torabi, F. Supervised deep learning-based paradigm to screen the enhanced oil recovery scenarios. *Sci. Rep.* **13**, 4892 (2023).
6. Ayoub, M. A., Tackie-Otoo, B. N. & Zulkefli, S. H. B. The combined effects of the minimum miscibility pressure and injection rate variations on recovery of co2 flooding in sandstone reservoir. *J. Petrol. Explor. Prod. Technol.* **12**, 2899–2913 (2022).
7. Tian, L. et al. Optimization of CO2 water-gas alternating injection-production parameters in low permeability reservoirs. in Volume 8: Offshore Geotechnics; Petroleum Technology V008T11A054 (American Society of Mechanical Engineers, Singapore, Singapore, 2024). https://doi.org/10.1115/OMAE2024-127862.
8. Vásquez Haro, H. A., Gomes, M. S. D. P. & Rodrigues, L. G. Numerical analysis of carbon dioxide injection into a high permeability layer for CO2-EOR projects. *J. Petrol. Sci. Eng.* **171**, 164–174 (2018).
9. Bakhshian, S., Bump, A. P., Pandey, S., Ni, H. & Hovorka, S. D. Assessing the potential of composite confining systems for secure and long-term CO2 retention in geosequestration. *Sci. Rep.* **13**, 21022 (2023).
10. AlRassas, A. M. et al. CO2 sequestration and enhanced oil recovery via the water alternating gas scheme in a mixed transgressive sandstone-carbonate reservoir: case study of a large middle East oilfield. *Energy Fuels*. **36**, 10299–10314 (2022).
11. Bonto, M. et al. Challenges and enablers for large-scale CO2 storage in chalk formations. *Earth Sci. Rev.* **222**, 103826 (2021).
12. Zareei, D., Rostami, B. & Kostarelos, K. Petrophysical changes of carbonate rock related to CO2 injection and sequestration. *Int. J. Greenhouse Gas Control*. **117**, 103648 (2022).
13. Wang, L. et al. Water-sensitive damage mechanism and the injection water source optimization of low permeability sandy conglomerate reservoirs. *Pet. Explor. Dev.* **46**, 1218–1230 (2019).
14. Li, J. et al. Optimization and evaluation of stabilizers for tight Water-Sensitive conglomerate reservoirs. *ACS Omega*. **7**, 5921–5928 (2022).
15. Wu, S. et al. Reservoir property changes during CO2–brine flow-through experiments in tight sandstone: implications for CO2 enhanced oil recovery in the triassic Chang 7 member tight sandstone, Ordos basin, China. *J. Asian Earth Sci.* **179**, 200–210 (2019).
16. Liu, P. & Zhang, X. Enhanced oil recovery by CO2–CH4 flooding in low permeability and rhythmic hydrocarbon reservoir. *Int. J. Hydrog. Energy*. **40**, 12849–12853 (2015).
17. Liu, Y., Nie, F., Zhang, B., Liu, T. & Hong, Y. The three-dimensional heterogeneous simulation study of CO2 flooding in low-permeability reservoirs. *Processes* **12**, 1843 (2024).
18. Deng, X. et al. Numerical simulation and parameter optimization for water-to-CO_2 flooding in a strongly water-sensitive reservoir. *ACS Omega*. **9**, 9655–9665 (2024).
19. Chaturvedi, K. R. & Sharma, T. Modified smart water flooding for promoting carbon dioxide utilization in shale enriched heterogeneous sandstone under surface conditions for oil recovery and storage prospects. *Environ. Sci. Pollut Res.* **29**, 41788–41803 (2022).
20. Zhao, Y. et al. Importance of conformance control in reinforcing synergy of CO2 EOR and sequestration. *Pet. Sci.* **19**, 3088–3106 (2022).
21. Wang, Q. et al. Effect of pore-throat microstructures on formation damage during miscible CO_2 flooding of tight sandstone reservoirs. *Energy Fuels*. **34**, 4338–4352 (2020).
22. Gandomkar, A. & Kharrat, R. Anionic surfactant adsorption through porous media in carbonate cores: an experimental study. *Energy Sour. Part A Recover. Utilization Environ. Eff.* **35**, 58–65 (2013).
23. Li, Y., Jiang, G., Li, X. & Yang, L. Quantitative investigation of water sensitivity and water locking damages on a low-permeability reservoir using the core flooding experiment and NMR test. *ACS Omega*. **7**, 4444–4456 (2022).
24. Gandomkar, A., Torabi, F., Nasriani, H. R. & Enick, R. M. Decreasing asphaltene precipitation and deposition during immiscible gas injection via the introduction of a CO2-soluble asphaltene inhibitor. *SPE J.* **28**, 2316–2328 (2023).
25. Hwang, J. & Pini, R. Supercritical CO2 and CH4 uptake by illite-smectite clay minerals. *Environ. Sci. Technol.* **53**, 11588–11596 (2019).
26. Torabi, F. & Gandomkar, A. Experimental evaluation of CO2-soluble nonionic surfactants for wettability alteration to intermediate CO2-oil wet during immiscible gas injection. *SPE J.* **29**, 5071–5086 (2024).
27. Parvizi Ghaleh, S., Khodapanah, E. & Tabatabaei-Nezhad, S. A. Experimental evaluation of thiamine as a new clay swelling inhibitor. *Pet. Sci.* **17**, 1616–1633 (2020).
28. Moslemizadeh, A., Khezerloo-ye Aghdam, S., Shahbazi, K. & Zendehboudi, S. A triterpenoid saponin as an environmental friendly and biodegradable clay swelling inhibitor. *J. Mol. Liq.* **247**, 269–280 (2017).
29. Hu, H. et al. Polyetheramine as swelling-inhibitor for expansive soil: performance and mechanism. *J. Appl. Polym. Sci.* **139**, 51639 (2022).
30. Renner, T. A. Measurement and correlation of diffusion coefficients for CO2 and rich-gas applications. *SPE. Reserv. Eng.* **3**, 517–523 (1988).

31. Upreti, S. R. & Mehrotra, A. K. Diffusivity of CO_2, CH_4, C_2 H_6 and N_2 in Athabasca bitumen. *Can. J. Chem. Eng.* **80**, 116–125 (2002).
32. Wang, L. S., Lang, Z. X. & Guo, T. M. Measurement and correlation of the diffusion coefficients of carbon dioxide in liquid hydrocarbons under elevated pressures. *Fluid. Phase. Equilibria*. **117**, 364–372 (1996).
33. Dong, X., Shi, Y., Huang, D. & Yang, D. Quantification of Preferential and mutual mass transfer of gases-light oil systems at high pressures and elevated temperatures by dynamic volume analysis. *Int. J. Heat Mass Transf.* **195**, 123188 (2022).
34. Basilio, E., Addassi, M., Al-Juaied, M., Hassanizadeh, S. M. & Hoteit, H. Improved pressure decay method for measuring CO2-water diffusion coefficient without convection interference. *Adv. Water Resour.* **183**, 104608 (2024).
35. Azin, R., Mahmoudy, M., Raad, S. & Osfouri, S. Measurement and modeling of CO2 diffusion coefficient in saline aquifer at reservoir conditions. *Open Engineering* **3**, (2013).
36. Wang, L. S. & Sun, C. Y. Diffusion of carbon dioxide in tetradecane. *J. Chem. Eng. Data*. **42**, 1181–1186 (1997).
37. Reamer, H. H., Opfell, J. B. & Sage, B. H. Diffusion coefficients in hydrocarbon systems methane-decane-methane in liquid phase - methane-decane-methane in liquid phase. *Ind. Eng. Chem.* **48**, 275–282 (1956).
38. Li, Z., Dong, M. & Shirif, E. Transient natural convection induced by gas diffusion in Liquid-Saturated vertical porous columns. *Ind. Eng. Chem. Res.* **45**, 3311–3319 (2006).
39. Li, Z. & Dong, M. Experimental study of carbon dioxide diffusion in Oil-Saturated porous media under reservoir conditions. *Ind. Eng. Chem. Res.* **48**, 9307–9317 (2009).
40. Gandomkar, A., Nasriani, R., Enick, H., Torabi, F. & R. M. & The effect of CO2-philic thickeners on gravity drainage mechanism in gas invaded zone. *Fuel* **331**, 125760 (2023).
41. Li, G. et al. Study on microscopic oil displacement mechanism of alkaline–surfactant–polymer ternary flooding. *Materials* **17**, 4457 (2024).
42. Prasad, S. K., Sangwai, J. S. & Byun, H. S. A review of the supercritical CO2 fluid applications for improved oil and gas production and associated carbon storage. *J. CO2 Utilization*. **72**, 102479 (2023).
43. Nematzadeh, M. et al. An experimental study of secondary WAG injection in a low-temperature carbonate reservoir in different miscibility conditions. *Pet. Sci. Technol.* **30**, 1359–1368 (2012).
44. Motealleh, M. et al. An experimental study on the applicability of water-alternating-CO_2 injection in the secondary and tertiary recovery in one Iranian reservoir. *Pet. Sci. Technol.* **30**, 2571–2581 (2012).
45. Aydin, H. & Akin, S. CO2 dissolution in the reservoir brine: an experimental and simulation-based approach. *Geothermics* **113**, 102774 (2023).
46. Hosein, R. & Alshakh, S. CO_2 sequestration in saline water: an integral part of CO_2 sequestration in a geologic formation. *Pet. Sci. Technol.* **31**, 2534–2540 (2013).
47. Wang, H. et al. Nonequilibrium dissolution behaviors and mass-transfer parameters for a CO2/heavy-oil system. *Chem. Eng. Sci.* **301**, 120746 (2025).
48. Jia, B., Tsau, J. S. & Barati, R. Measurement of CO2 diffusion coefficient in the oil-saturated porous media. *J. Petrol. Sci. Eng.* **181**, 106189 (2019).
49. Amarasinghe, W., Fjelde, I., Giske, N. & Guo, Y. CO2 convective dissolution in oil-saturated unconsolidated porous media at reservoir conditions. *Energies* **14**, 233 (2021).
50. Gandomkar, A. & Kharrat, R. The tertiary FAWAG process on gas and water invaded zones: an experimental study. *Energy Sour. Part A Recover. Utilization Environ. Eff.* **34**, 1913–1922 (2012).
51. Thorstenson, D. C. & Pollock, D. W. Gas transport in unsaturated porous media: the adequacy of fick's law. *Rev. Geophys.* **27**, 61–78 (1989).
52. Rezk, M. G., Foroozesh, J., Abdulrahman, A. & Gholinezhad, J. CO_2 diffusion and dispersion in porous media: review of advances in experimental measurements and mathematical models. *Energy Fuels*. **36**, 133–155 (2022).
53. Bouillard, N., Eymard, R., Herbin, R. & Montarnal, P. Diffusion with dissolution and precipitation in a porous medium: mathematical analysis and numerical approximation of a simplified model. *ESAIM: M2AN*. **41**, 975–1000 (2007).

Acknowledgements

The authors gratefully acknowledge the financial support from the Key Research Project of Heilongjiang Province (2023ZXJ06A01), National Natural Science Foundation of China(52304026) and Daqing Science and Technology Innovation Guidance Project (YZ-XS-202312-10).

Author contributions

Conceptualization: M.Z, and J.W; Resource: M.Z, and J.W.; Data curation: M.Z, L.C, B.L, X.Y, and Y.H; Formal analysis: M.Z, J.W, and L.C; supervision: M.Z, and J.W.; Funding acquisition: J.W, F.S, and C.Z.; Validation: M.Z, B.L, and X.Y.; Investigation: M.Z, and L.C.; Methodological: M.Z, L.C, and Y.H.; Writing – original draft: M.Z.; Project management: J.W, and F.S.; Manuscript review and revision: M.Z, and J.W.

Funding

This study was funded by the Key Scientific Research Project of Heilongjiang Province (2023ZXJ06A01), National Natural Science Foundation of China(52304026) and Daqing Science and Technology Innovation Guidance Project (YZ-XS-202312-10).

Declarations

Competing interests

The authors declare no competing interests.

Additional information

Correspondence and requests for materials should be addressed to J.W.